Investigation on microstructure, energy gap, photoluminescence and magnetic studies of Co and Cu in situ doped ZnO nanostructures

C. Prabakar[1], S. Muthukumaran[1,*] , and V. Raja[1]

[1] PG & Research Department of Physics, Government Arts College, Melur, Madurai, Tamilnadu 625 016, India

ABSTRACT

Co (3%)-doped ZnO and Co, Cu (Co = 3% and Cu = 2 to 4%) dual-doped ZnO nanostructures were prepared using chemical co-precipitation route. The structural analysis indicated no alteration in the structure of hexagonal ZnO and the absence of secondary/impurity phases induced by Co/Cu addition into ZnO. The reduction of crystallite size ($\approx$ 25 nm) at Cu = 2% is due to the suppression of growth rate and the dissimilarities between Co^{2+}/Cu^{2+} and Zn^{2+} ions, and the enhanced crystallite size ($\approx$ 29 nm) at Cu = 4% is responsible for the more defect sites associated with interstitials and vacancies of Co^{2+} and Cu^{2+} in Zn–O lattice. The persistent c/a ratio ($\sim$ 1.602) signified the absence of structural modification by Co/Cu substitution for Zn. The decrease in optical absorption, increase in transmittance and the enhanced energy gap of ZnO by Co/Cu addition were discussed by consideration of dopants and the stimulated defect states. The continuous widening of energy gap ($\Delta E_g \approx$ 0.08 eV) with Cu substitution is clarified using Burstein–Moss (BM) band filling effect through energy-level diagram. The existence of Zn–O and Zn–Co/Cu–O bondings around $\approx$ 442–468 cm^{-1} was verified by Fourier transform infra-red analysis. The elevated intensity ratio between green and ultra-violet photoluminescence (I_G/I_{UV}) at higher Cu concentration, Cu = 4% ($\approx$ 0.74), revealed the occurrence of higher number of defects, particularly oxygen-related defect states, in (Zn, Co, Cu)O lattice. The observed room temperature ferromagnetism (RTFM) in Co, Cu-doped ZnO nanostructures is discussed based on the oxygen vacancy-mediated bound magnetic polarons (BMP) and the exchange interaction between the free electrons and local spin-polarized electrons.

Address correspondence to E-mail: drsmk123@yahoo.co.in

1 Introduction

In recent times, nanostructured materials are applied for energy storage and photocatalytic applications due to their unique properties [1–6]. The semiconducting nanostructures of ZnO have received a large amount of credit as a probable candidate in the field like solar energy conversion, different luminescence, varistors, transparent UV protection films, different type of sensors, spintronic applications, etc. [7–12], owing to their abnormal electrical, mechanical, optical, and magnetic characteristics which originates from the size-dependent quantum effects. Doping of semiconducting materials by impurity elements attained their extensive technological and scientific applications in nanoelectronics and opto-electronics [13], and nanomaterials doped with magnetic elements are of attention for their significant applications in spin-dependent electronic instruments [14].

Many of the diluted magnetic semiconductors (DMS) which have numerous applications in spintronic and opto-electronics [15–17] were obtained by transition metal (TM) doping to ZnO. The addition of 3d-TM into ZnO is the effective way to improve not only the optical, structural and luminescence properties [18, 19] and also to create the excellent candidate to accomplish Curie temperature around room temperature [20, 21]. The most usually used TMs in Zn–O host lattice are Co, Al, Cu, Sn, etc. [22–26]. Along with the diverse doping elements, Cu and Co have more significance because (i) they are a well-known luminescence emission activators, which can adjust the emission wavelength and intensity of ZnO by generating different localized impurity levels [27], (ii) they have comparable electronic shell structure, chemical and physical characteristics to those of Zn [28], and (iii) they can modify the morphology of the material and hence the optical characteristics of the ZnO nanostructures [24].

The grain size reduction and cell parameter shrinkage were reported by Arshad et al. with the increase in Co content in ZnO nanostructures [29]. A characteristic room-temperature ferromagnetic (RTFM) nature has been detected in $Zn_{1-x}Co_xO$ material by Wang et al. [30], and they suggested that the solid solution of Co in ZnO plays a main role in generation of noticed ferromagnetic behavior. Nirmal and Anukaliani [31] showed the excellent anti-bacterial activity, especially for S. aureus in Co-doped ZnO. Lee et al. [32] reported that the single-phase hexagonal structure was observed only up to Co = 5% in $Zn_{1-x}Co_xO$ nanosystem and, above the Co = 5% level, the secondary phases like CoO, Co_3O_4 and Co metal clusters appeared. Therefore, in the present work, Co is chosen as the first doping element into ZnO and its level is limited to 3% ($Zn_{0.97}Co_{0.03}O$) to avoid the secondary-phase formation [33].

The structural and magnetic behavior of $Zn_{0.90}Co_{0.10}O$ nanostructures synthesized using the co-precipitation method has been studied by Chakraborti et al. [34], and they indicated that the inherent free electrons were accountable for the ferromagnetic nature in the Co, Cu dual-doped ZnO. Hou et al. [35] reported that the transition temperature of $Zn_{0.98}Cu_{0.02}O$ is found to be around 350 K which is decreased to 320 K with nitrogen addition [35]. The effect of shape, size and hydrogenation on FM nature of $Zn_{0.93}Co_{0.05}Cu_{0.02}O$ nanostructures at room temperature was established by Xu et al. [36]. RTFM was noticed in $Zn_{0.94}Co_{0.05}Cu_{0.01}O$ from DC magnetization as well as resistivity measurement that can be accredited to the creation of additional charge carriers in Co-substituted ZnO by Cu doping [37]. The relation involving the growth of ZnO system and the positions of Co and Cu dopants was determined by means of the mobility and energy formation of the doping atoms [38].

Ag and Cd with PVP-based ZnO composite were prepared by Vignesh et al. [39] which could modify the band gap of ZnO and enhanced the charge-carrier separation and less recombination rate. The Sn:Cu:ZnO nanoparticles were synthesized by Shanmugam et al. [40] using microwave-assisted precipitation method. They observed better photocatalytic and antibacterial behavior for Sn:Cu:ZnO nanoparticles. The chemical composition, deep morphology, structure, optical absorption and photocatalytic properties of the as-obtained $g-C_3N_4/MoS_2/Bi_2O_3$ -photocatalysts were discussed by Shanmugam et al. [41]. The antibacterial activity of the $gC_3N_4–BiFeO_3–Cu_2O$ nanocomposite showed a well deactivation in both G^+ (S. aureus) and G^- (E. coli) bacteria's when compared to other samples [42]. Improving visible-light active photocatalytic performance of the heterostructured $g–C_3N_4–V–TiO_2$ (g–C3N4–Vanadium–TiO2) hybrid catalyst has been synthesized via facile calcination by Shanmugam et al. [43]. Improved antibacterial activity against the bacterial strains was clearly observed when adding Ce dopant to the SnO_2 [44]. The photocatalytic performances of 4% of Zr-

doped SnO_2 nanoparticles (NPs) were thoroughly explored in the photodegradation of methyl orange (MO) dye, thus revealing higher photocatalytic activity in the degradation of MO than pristine and 2% of Zr-doped SnO_2 under via visible-light exposure [45].

Lin et al. described that a minute amount of Cu doping into ZnO generates the more number of free charge carriers [46]. In contrast, the additional doping of Cu induces the secondary phase (CuO) in Zn–O lattice and thus reduces the free charge carrier concentration [47]. However, the dominant part of research findings was made on Cu and Co dual-doped ZnO thin-film system [36–47] and the complete investigation of the structural, photoluminescence and magnetic properties on Cu and Co dual-doped ZnO nanostructures is still scanty.

Within the various physical and chemical techniques existing in the preparation of TM-doped ZnO [48–52], the co-precipitation method is selected to prepare Co and Cu dual-doped ZnO since it is one of the significant methods to synthesize the nanostructures in large scale with low cost. Therefore, in the current work, $Zn_{0.97-x}Co_{0.03}Cu_xO$ $(0 \leq x \leq 0.04)$ nanostructures were prepared by the co-precipitation technique and the influence of Cu on their optical, photoluminescence and magnetic properties was investigated in detail. Since the addition of Co and Cu into ZnO primary system induces the secondary phases at higher doping levels, the Co and Cu contents are limited to 3% and 4% [53–56], respectively.

2 Materials and experimental procedure

2.1 Preparation of $Zn_{0.97-x}Co_{0.03}Cu_xO$ (x = 0, 0.02 and 0.04) nanostructures

For the synthesis of $Zn_{0.97-x}Co_{0.03}Cu_xO$ (x = 0, 0.02 and 0.04) nanostructures, the suitable amounts of zinc acetate dihydrate [$Zn(CH_3CO_2)_2.2H_2O$, source of Zn^{2+}, anions], cobalt (III) acetate tetrahydrate ($Co(CH_3CO_2)_3.4H_2O$, source of Co^{2+}) and copper (II) acetate monohydrate ($Cu(CH_3CO_2)_2.H_2O$, source of Cu^{2+}, anions) are used as metal precursors. Sodium hydroxide (NaOH) is used to control the pH value. The prepared NaOH solution was added dropwise to the initial solution to increase the pH to 8.5. The chemicals used in the current work were in analytical grade (AR) with 99.99% purity purchased from M/s.

Merck. Ultrapure deionized water was used as solvent throughout the synthesis process.

Initially, appropriate amount of $Zn(CH_3CO_2)_2.2H_2O$, $Co(CH_3CO_2)_3.4H_2O$ and $Cu(CH_3CO_2)_2.H_2O$ was dissolved in double-distilled water and kept under a constant stirring until clear solution was achieved. NaOH solution was prepared separately by dissolving appropriate amount of NaOH in 50 ml double-distilled water. The prepared NaOH solution was added dropwise into the initial solution under constant stirring at room temperature until pH of the solution became 8.5. The mixed solution was stirred for another 2 h. The preparative method was described in the previous contribution [30]. The gelatinous precipitates were filtered and washed several times to remove the impurities. The final precipitates were dried using an oven at 80 °C for 2 h. The dried precipitates were collected and grounded using an agate mortar. Finally, the synthesized nanoparticles were annealed at 500 °C in the air atmosphere for 2 h followed by furnace cooling. The same procedure was repeated to the remaining Cu concentrations (x = 0, 0.02 and 0.04). The chemicals used to synthesize $Zn_{0.97-x}Co_{0.03}Cu_xO$ (x = 0, 0.02 and 0.04) nanostructures with their chemical formulae are presented in Table 1.

2.2 Characterization technique

The crystal structure of $Zn_{0.97-x}Co_{0.03}Cu_xO$ (x = 0, 0.02 and 0.04) nanostructures was determined by powder X-ray diffraction method. The X-ray diffraction (XRD) patterns were recorded by RigaKu C/max-2500 diffractometer using Cu Kα radiation (λ = 1.5406 Å) at 40 kV and 30 mA from 2θ = 30° to 70°. The surface morphology was studied using a scanning electron microscope (SEM, JEOLJSM 6390). The elemental composition present in the sample was determined by energy-dispersive X-ray (EDX) spectrometer. The microstructure was also examined by transmission electron microscopy (TEM). The UV–Visible optical absorption study was carried out to explore their optical properties. The optical absorption and transmittance were determined using an UV–Visible spectrometer (Model: lambda 35, Make: PerkinElmer) from 300 to 500 nm. The chemical bonding was studied by a Fourier transform infrared (FTIR) spectrometer (Model: PerkinElmer, Make: Spectrum RX I) from 400 to 4000 cm^{-1}. The sample used for FTIR studies is in the form of pellets

Table 1 Chemicals used to synthesize $Zn_{0.97-x}Co_{0.03}Cu_xO$ (x = 0, 0.02 and 0.04) nanostructures with their chemical formulae

| Samples	Chemicals	Chemical formulae
Co = 3% doped ZnO	Zinc acetate dihydrate	$Zn(CH_3CO_2)_2.2H_2O$
	Cobalt *(III)* acetate tetrahydrate	$Co(CH_3CO_2)_3.4H_2O$
	Sodium hydroxide	NaOH
Co = 3% and Cu = 2 or 4% dual doped ZnO	Zinc acetate dihydrate	$Zn(CH_3CO_2)_2.2H_2O$
	Cobalt *(III)* acetate tetrahydrate	$Co(CH_3CO_2)_3.4H_2O$
	Copper (II) acetate monohydrate	$Cu(CH_3CO_2)_2.H_2O$
	Sodium hydroxide	NaOH

prepared by mixing the nanoparticles with KBr at 1 weight %. The room temperature photoluminescence (PL) spectra were recorded over the wavelength range from 350 to 600 nm using a fluorescence spectrophotometer (Model: Hitachi, Make: F-2500) at excitation wavelength of 330 nm and power of 150 W to study the radiative recombination properties. The magnetization (M) and magnetic hysteresis (M–H) loops were measured at room temperature using a vibrating sample magnetometer (VSM, Make: Lake shore, Model: 7404).

3 Results and discussion

3.1 XRD: structural studies

XRD analysis is among the most important characterization techniques for analyzing phase and structure of the synthesized samples. Moreover, the crystallite size, micro-strain and other lattice parameters also can be estimated by the evaluation of X-ray diffraction patterns. The XRD spectra of $Zn_{0.97-}$ $Co_{0.03}O$, $Zn_{0.95}Co_{0.03}Cu_{0.02}O$ and $Zn_{0.93}Co_{0.03}Cu_{0.04}O$ samples for the diffraction angle range of 30°–70° are shown in Fig. 1. Totally nine XRD peaks are detected along all three samples. The XRD reflexes of $Zn_{0.97-}$ $Co_{0.03}O$ sample located at the angles 31.7, 34.2, 36.1, 46.7, 56.5, 62.7, 66.2, 67.9 and 69.2° corresponding to (100), (002), (101), (102), (110), (103), (200), (112) and (201) planes, respectively [57]. Among the diffraction orientations, (101) reflex is selected to derive the size and other structural parameters due to its higher intensity. The obtained XRD patterns are in a good relation with the characteristic JCPDS file of ZnO (JCPDS Card No. 00-001-1136) which confirmed the wurtzite-type structure of the sample. The similar experimental results were reported by Hu et al. [58]
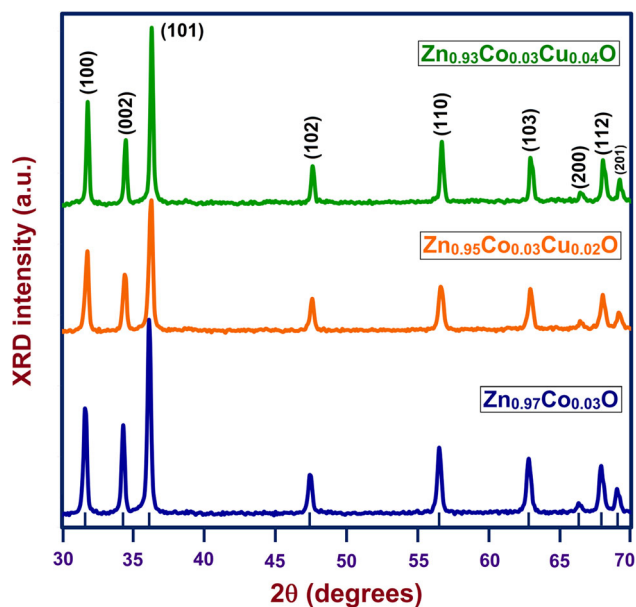

Fig. 1 XRD pattern of $Zn_{0.97-x}Co_{0.03}Cu_xO$ nanostructure with different Cu doping levels from 0 to 4% between the angles 30° and 70°

for $Zn_{0.95-x}Co_{0.05}Cu_xO$ structure. The sharp XRD peaks pointed out the good crystalline nature of the samples. No foreign XRD peaks corresponding to Co or Cu metals/oxides/secondary binary phases are detected within the sensitivity limit of XRD measurements, and it reflects the phase purity of the samples and also the proper substitution of Cu into Zn–Co–O lattice. Earlier, Mukhtar et al. [59] reported the existence of similar trend ZnO:Cu system up to Cu doping level around 11 at. %.

Among the nine detected peaks, (100), (002) and (101) reflexes exhibit strong and prominent intensities. The magnified XRD spectra of Zn_0 $Zn_{0.97}Co_{0.03}O$, $Zn_{0.95}Co_{0.03}Cu_{0.02}O$ and $Zn_{0.93}Co_{0.03}Cu_{0.04}O$ nanostructures for the diffraction angles from 31° to 37°, which include reflexes (100), (002) and (101), are

presented in Fig. 2. The primary addition of Cu ($Zn_{0.95}Co_{0.03}Cu_{0.02}O$, Cu = 2%) reduced the peak intensity, as compared to that of $Zn_{0.97}Co_{0.03}O$ (Cu = 0%), and the further addition of Cu increases the peak intensity. A same decreasing trend of peak intensity has been described by Peng et al. [60] and Sreedhar et al. [61] in Cu-doped ZnO system. This reduction is attributed to the influence of defects or disorder generated by the Cu^{2+} ions substituted in the ZnO lattice [62]. In addition to the peak intensity modulation, the (101) peak position shifted continuously to higher angles by Cu addition. The similar peak shift toward higher angles is supported by the literature [63–65]. The noticed moderate decrease in intensity and also the shift toward higher angle side at Cu = 2% are accredited to the reduction in size owing to the substitution of Zn^{2+} ions by smaller Cu^{2+} ions, which proposes that Cu^{2+} ions can replace Zn^{2+} into Zn–O lattice [66, 67], with no modification in the host ZnO crystal structure [68]. Even though the peak shift to higher angles continued throughout
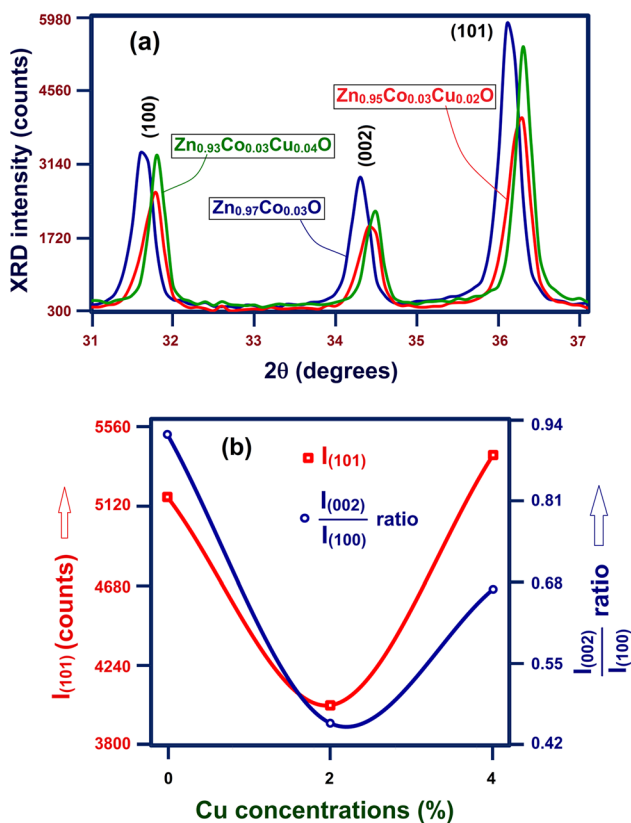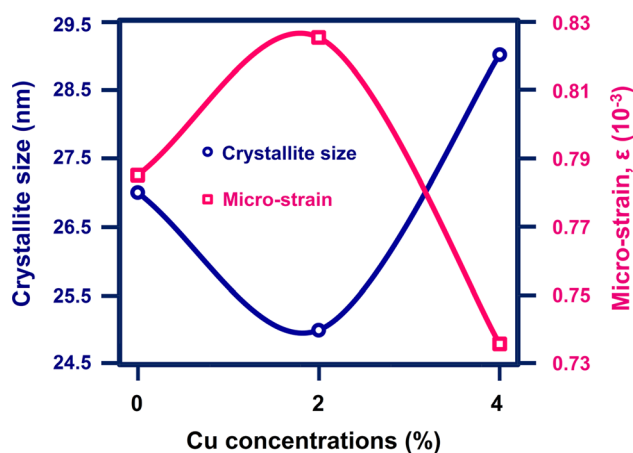
the Cu content increase, the peak intensity increased at Cu = 4% after showing a significant reduction at Cu = 2%. The observed increase in intensity after Cu = 2% is due to the creation of new nucleating centers and defect sites at higher Cu levels [69].

The modification in intensity of (101) reflex and the intensity ratio of (002) and (100) reflexes at different Cu concentrations from 0 to 4% are given in Fig. 2b. Usually, the peak intensity and peak position are dependent on the various factors such as crystallite size, micro strain and inter-planar distance. The attained intensity ratio of (002) and (100) reflexes is nearly equal to 1 for single Co-doped ZnO ($Zn_{0.97}Co_{0.03}O$) which represent the existence of spherical-shaped grains, as shown in SEM micrographs (Figs. 4 and 5). The noticed lower intensity ratio in Cu/Co dual-doped ZnO sample represents the alteration of size and shape of the grains.

The crystallite size and micro-strain as a function of Cu content are given in Fig. 3. Here, the crystallite size (D) is obtained using Scherrer's formula [70] $D = 0.9\lambda/\beta\cos\theta$. The micro-strain ($\varepsilon$) was estimated using the relation [71], $\varepsilon = \beta\cos\theta/4$. In Table 2, the peak position (2θ), peak intensity, full width at half maximum (FWHM) of (101) reflex, average crystallite size (D) and micro-strain (ε) are listed for the $Zn_{0.97-x}Co_{0.03}Cu_xO$ ($0 \leq x \leq 0.04$) nanostructures. The reduction in size at Cu = 2% is owing to distortion in the basic Zn–O lattice by the Cu^{2+} doping which reduce the nucleation and hence the growth rate up to Cu = 2% [72, 73]. The observed decrease in size is consistent with the literature [74]. Both the

Fig. 2 a Enlarged view of XRD pattern from 31° to 37° which includes (100), (002) and (101) planes, b variation of intensity along (101) plane and intensity ratio between (002) and (100) plane for different Cu levels from 0 to 4%

Fig. 3 The variation in crystallite size and micro-strain of $Zn_{0.97-x}Co_{0.03}Cu_xO$ nanostructure with different Cu doping levels from 0 to 4%

Table 2 The variation of peak position (2θ), peak intensity, full width at half maximum (FWHM), average crystallite size (D) and micro-strain (ε) of $Zn_{0.97-x}Co_{0.03}Cu_xO$ ($0 \leq x \leq 0.04$) nanostructures

Samples	Peak position, 2θ (Degree)	Peak intensity (counts)	FWHM, β (degrees)	Average crystallite size, D (nm)	Micro-strain, ε (10^{-3})
$Zn_{0.97}Co_{0.03}O$	36.10	5830	0.310	27	0.785
$Zn_{0.95}Co_{0.03}Cu_{0.02}O$	36.22	4038	0.335	25	0.825
$Zn_{0.93}Co_{0.03}Cu_{0.04}O$	36.28	5402	0.290	29	0.736

increase in FWHM and the enhanced micro-strain are responsible for the present shrinkage in crystallite size at Cu = 2% [69]. The further increase in Cu content generates the additional defects and lattice deformation. The presence of high intensity defects is responsible for the enhanced crystallite size at Cu = 4% [75]. The increase in size after Cu = 2% is due to the decrease in micro-strain and FWHM [76] as noticed in Table 2.

Table 3 illustrates the modification in lattice constants such as inter-planar distance 'd', 'a' and 'c' values, c/a ratio and volume per unit cell of Co, Cu-doped ZnO with different Cu content from 0 to 4%. The cell parameter 'd' is obtained from Bragg's equation, $2d \sin \theta = n\lambda$ where 'θ' is the angle of diffraction [77]. The cell parameters 'a' and 'c' were derived using the lattice relation [78], $1/d^2 = 4/3 ((h^2 + hk + k^2)/a^2) + l^2/c^2$, and the volume per unit cell is obtained from the relation [79], volume (V) = $0.866 \times a^2 \times c$. The change in '$d$' value and lattice parameters are depending on doping elements, the defects induced by dopant, the difference in ionic radii and the induced strain or stress by doping element [80]. The obtained lower lattice parameters, 'd' value and volume per unit cell at Cu $\leq$ 4% are possibly due to the substitution of Cu^{2+} instead of Zn^{2+} (0.74 Å) [81] in Zn–Co–Cu–O lattice. The similar decreasing trend of lattice parameters at lower Cu concentrations was noticed by Liu et al. [82] which is consistent with the present results. The persistent c/a ratio ($\sim$ 1.602) signified the absence of structural modification by Co/Cu substitution for Zn. The

changes in lattice parameters, diffraction intensity, shift of peak positions and crystallite size confirm the substitution of Co and Cu in Zn–O lattice [83, 84].

3.2 SEM and TEM: microstructural studies

The influence of Cu doping on the surface morphology, size and shape of the particles or grains in Co, Cu dual-doped ZnO was analyzed using SEM micrographs. Figure 4a illustrates the surface morphology of $Zn_{0.97}Co_{0.03}O$ nanostructure which shows the agglomerated spheroid like particle structure with un-even grain size distribution. The current spherical shape is supported by the intensity ratio along (002) and (100) planes as shown in Fig. 2b. The doping of Cu (Cu = 2%) slightly reduces the size of the particles which is pointed out in Fig. 4b. The reduction in size is associated with the nucleation mechanism in the growth process. The addition of Cu controls the nucleation rate, hindering the growth rate in the Zn–Co–Cu–O lattice due to the dissimilarities in the ionic radius between Cu^{2+} and Zn^{2+} ions [85, 86]. This is confirmed by the XRD spectra which reflect the de-generated crystallization by Cu doping. Moreover, the reduction of size is useful to improve the photocatalytic performance [87]. Figure 4c displays the morphology of Cu = 4%. Even though no significant alteration is noticed in shape of the grains, the size is enhanced moderately due to the generation of defect states.

For better visualization toward the microstructure, TEM micrographs are carried out and presented in

Table 3 The variation of d value, cell parameters 'a' and c, c/a ratio and volume (V) of $Zn_{0.97-x}Co_{0.03}Cu_xO$ ($0 \leq x \leq 0.04$) nanostructures

Samples	d value (Å)	Cell parameters (Å)		c/a ratio	Volume, V (Å)^3
		$a = b$	c		
$Zn_{0.97}Co_{0.03}O$	2.4860	3.2660	5.2284	1.601	48.2951
$Zn_{0.95}Co_{0.03}Cu_{0.02}O$	2.4783	3.2540	5.2119	1.602	47.7918
$Zn_{0.93}Co_{0.03}Cu_{0.04}O$	2.4742	3.2483	5.2036	1.602	47.5488
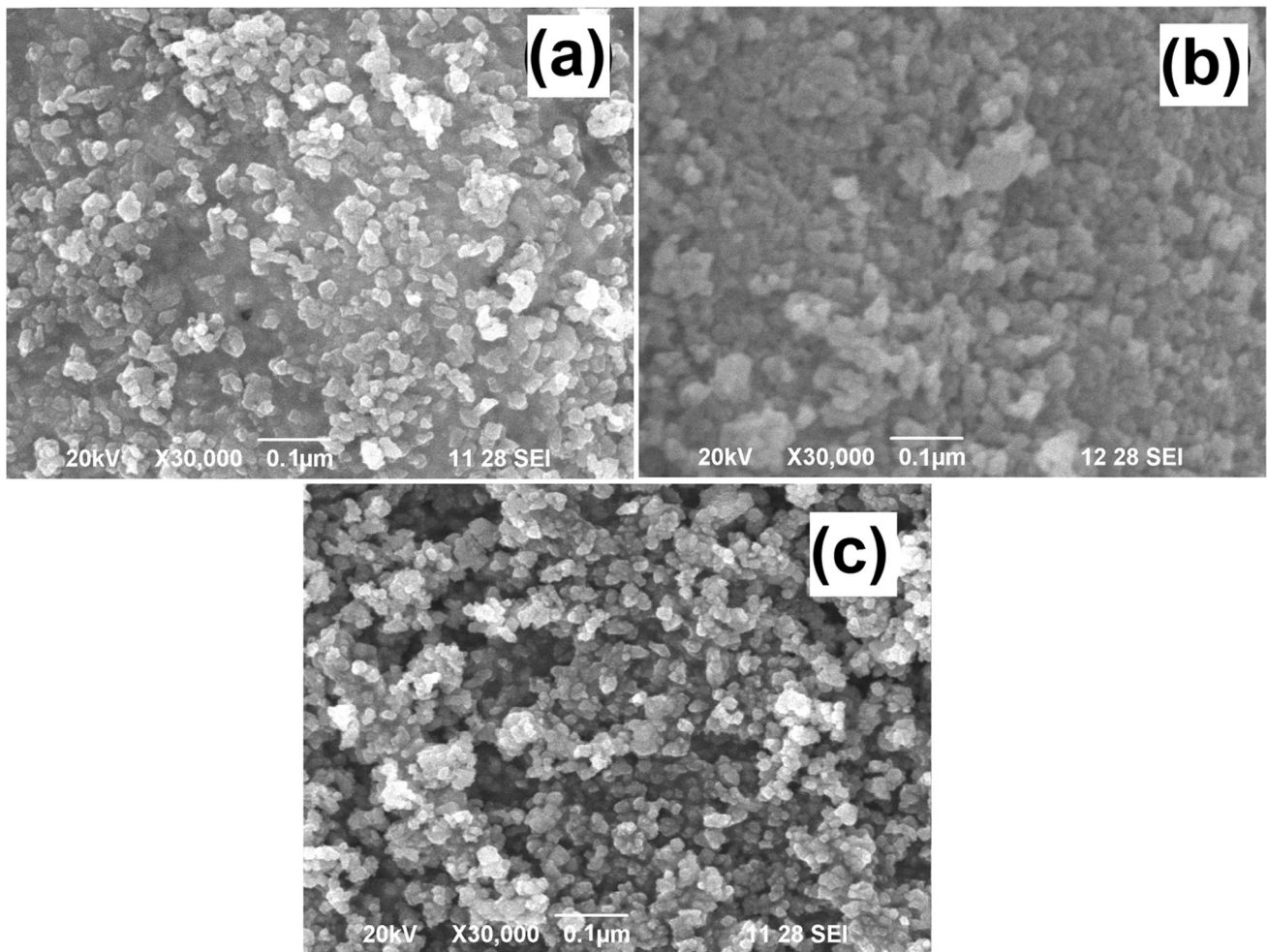
Fig. 4 SEM images of **a** $Zn_{0.97}Co_{0.03}O$, **b** $Zn_{0.95}Co_{0.03}Cu_{0.02}O$ and **c** $Zn_{0.93}Co_{0.03}Cu_{0.04}O$ nanoparticles

Fig. 5. Figure 5a shows the microstructure of $Zn_{0.97-}Co_{0.03}O$ (Cu = 0%) sample which is mostly composed of quasispherical-like structure with nonuniform particle size around 20–35 nm. The shape of particles is significantly modified by Cu = 2% addition as shown in Fig. 5b which includes some rod-like structure. In addition to the alteration in shape, the size also reduced by Cu = 2% addition. Figure 5c displays the TEM micrograph of Cu = 4% added sample with enhanced particle size which may be due to the effect of more defects existing at higher Cu concentrations.

3.3 EDX: compositional analysis

EDX spectra have been taken out in order to analyze and validate the existence of Cu, Co and Zn in $Zn_{0.97}Co_{0.03}O$, $Zn_{0.95}Co_{0.03}Cu_{0.02}O$ and $Zn_{0.93}Co_{0.03}-Cu_{0.04}O$ nanostructures. Figure 6a–c shows the EDX

spectra of $Zn_{0.97}Co_{0.03}O$, $Zn_{0.95}Co_{0.03}Cu_{0.02}O$ and $Zn_{0.93}Co_{0.03}Cu_{0.04}O$ nanostructures, respectively. The insert of Fig. 6 provides the atomic % of the basic constitutional elements such O, Co, Cu and Zn. The experimentally derived atomic % of the compositional elements such as Zn, Co, Cu and O present in $Zn_{0.97-x}Co_{0.03}Cu_xO$ (Cu = 0, 2 and 4%) nanostructures is presented in Table 4. No additional peaks associated with metal or oxides other than Co, Cu, Zn and O identified from Fig. 6 convey the substance purity of the samples. The attained atomic % of Co/(Zn + Co + Cu) ratio is found to be 3.05%, 2.99% and 3.10% for $Zn_{0.97}Co_{0.03}O$, $Zn_{0.95}Co_{0.03}Cu_{0.02}O$ and $Zn_{0.93}Co_{0.03}Cu_{0.04}O$ nanostructures, respectively. Likewise, the ratio of Cu/(Zn + Co + Cu) in $Zn_{0.95-}Co_{0.03}Cu_{0.02}O$ and $Zn_{0.93}Co_{0.03}Cu_{0.04}O$ nanostructures is estimated as 1.96% and 4.06%, respectively. Since the derived atomic % of Cu and Co ratio is more or less equal to their nominal stoichiometry within the
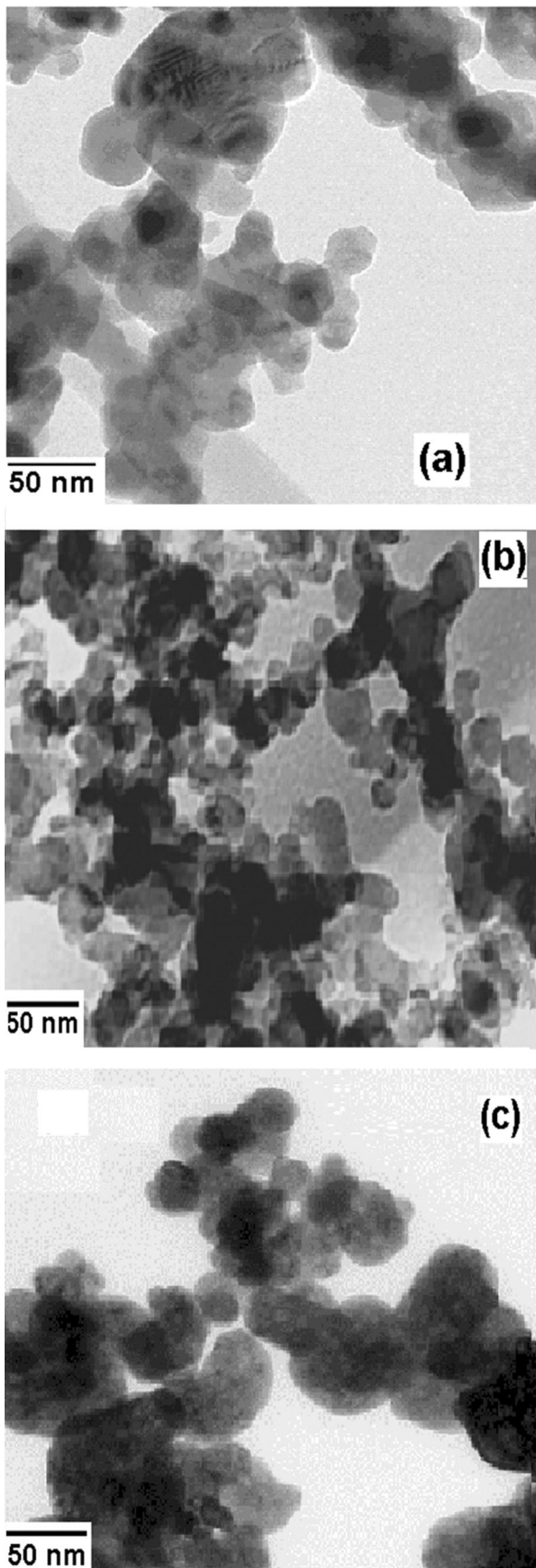
◀**Fig. 5** TEM images of **a** $Zn_{0.97}Co_{0.03}O$, **b** $Zn_{0.95}Co_{0.03}Cu_{0.02}O$ and **c** $Zn_{0.93}Co_{0.03}Cu_{0.04}O$ nanoparticles

experimental error, the EDX analysis confirms the real doping of Co and Cu in Zn–O lattice.

3.4 Optical absorption and transmittance spectra

The optical absorption spectra of $Zn_{0.97-x}Co_{0.03}Cu_xO$ nanostructures with various Cu levels from 0 to 4% have been made between the wavelengths 300 and 500 nm in order to analyze and visualize the variation in optical absorption. Figure 7a shows the absorption variation in $Zn_{0.97}Co_{0.03}O$, $Zn_{0.95}Co_{0.03}Cu_{0.02}O$ and $Zn_{0.93}Co_{0.03}Cu_{0.04}O$ nanostructures, and they have highest absorption in the UV range and sharply drop off around 350 nm. The present sharp decrease in absorption is represented as absorption edge/cutoff wavelength which reveals the optical band gap of the samples. The current strong absorption in the UV wavelength is corresponding to the transition of electrons from valance level into conduction level by absorbing UV light [88]. No anomalous absorption bands detected in the present study express the prepared samples are the direct band gap semiconductors.

Both the absorption intensity and the absorption bands depend on the different features such as energy gap, oxygen interstitials/deficiency, surface roughness and defect centers [89]. $Zn_{0.97}Co_{0.03}O$ sample exhibits highest absorption intensity. The substitution of Cu = 2% into $Zn_{0.97}Co_{0.03}O$ not only made the slight reduction in absorption intensity also shift the absorption edge toward the lower angle side as shown in Fig. 7a. The current shift of absorption edge toward the lower wavelength region is largely due to the reduction of crystallite size [90]. The absorption intensity declines further with the increase in Cu level (Cu = 4%), but the shift of absorption edge continues along lower wavelength side. The further reduction in intensity at Cu = 4% is associated with the generation of more defect by Co/Cu addition [91].

Figure 7b represents the optical transmittance variation in $Zn_{0.97}Co_{0.03}O$, $Zn_{0.95}Co_{0.03}Cu_{0.02}O$ and $Zn_{0.93}Co_{0.03}Cu_{0.04}O$ nanostructures between the wavelengths range from 300 to 500 nm. The noticed transmittance near-UV region along all the samples is
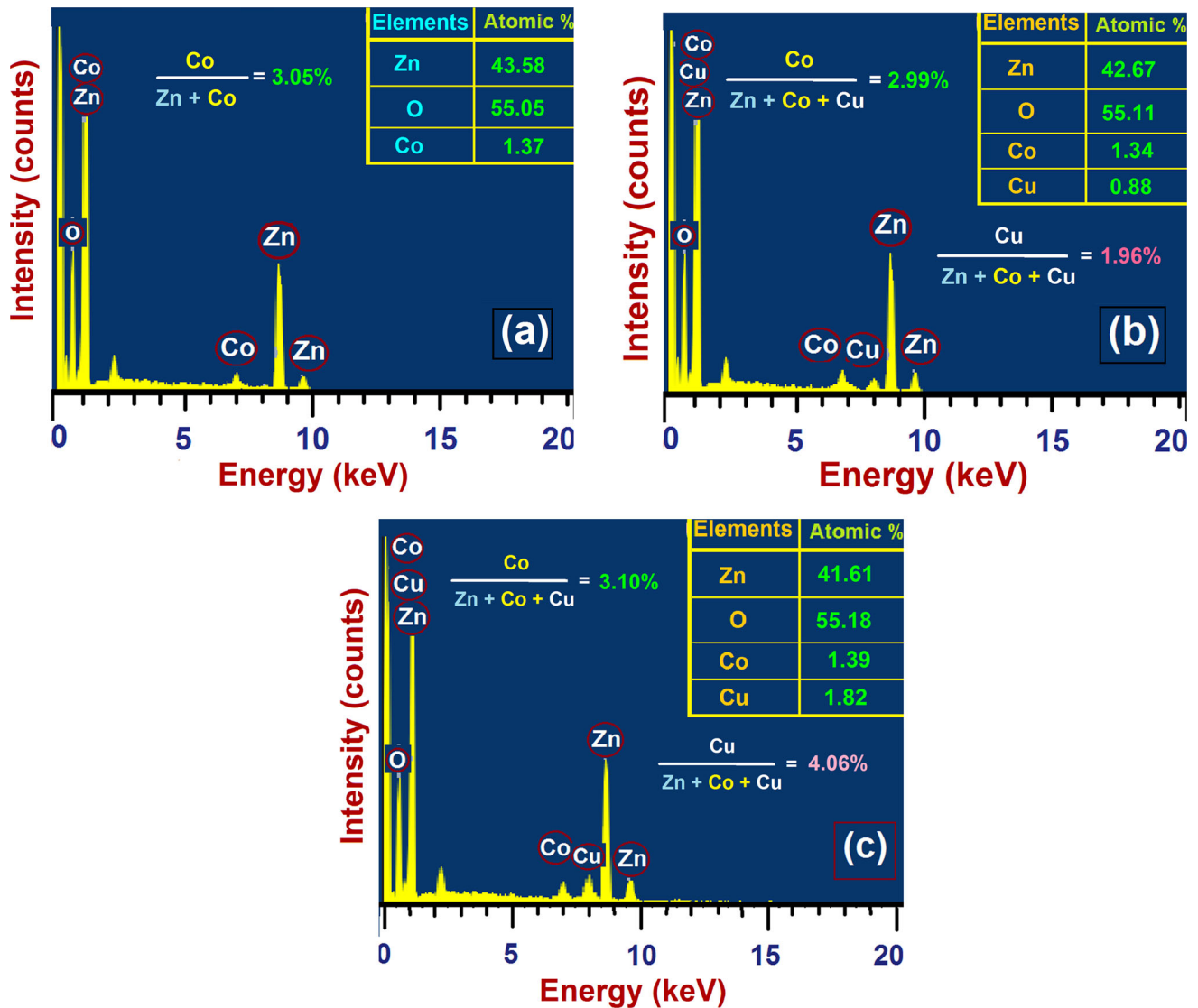
Fig. 6 EDX spectra of **a** $Zn_{0.97}Co_{0.03}O$, **b** $Zn_{0.95}Co_{0.03}Cu_{0.02}O$ and **c** $Zn_{0.93}Co_{0.03}Cu_{0.04}O$ nanoparticles. The inset shows the atomic percentage of the constituent elements

Table 4 The quantitative analysis of the compositional elements present in the different $Zn_{0.97-x}Co_{0.03}Cu_xO$ ($0 \leq x \leq 0.04$) nanostructures using EDX analysis

Samples	Atomic percentage of the elements (%)					
	Zn	O	Co	Cu	Co /(Zn + Co + Cu)	Cu /(Zn + Co + Cu)
$Zn_{0.97}Co_{0.03}O$	43.58	55.05	1.37	–	3.05	–
$Zn_{0.95}Co_{0.03}Cu_{0.02}O$	42.67	55.11	1.34	0.88	2.99	1.96
$Zn_{0.93}Co_{0.03}Cu_{0.04}O$	41.61	55.18	1.39	1.82	3.10	4.06

lower than visible wavelength region and exhibits a sharp fall off of absorption edge. The current lower transparencies are due to the transition of electrons between the valence band and conduction band. Moreover, the ultra-violet radiation has the smaller wavelength, and hence, it might be scattered by means of smaller defects [28]. In the visible region, the energy of the radiation is below the energy gap of the material and hence the wavelength of the light is greater than the crystallite size/pore size/mean surface roughness [61]. As a result, in the visible range, the scattering is negligible and hence the loss of
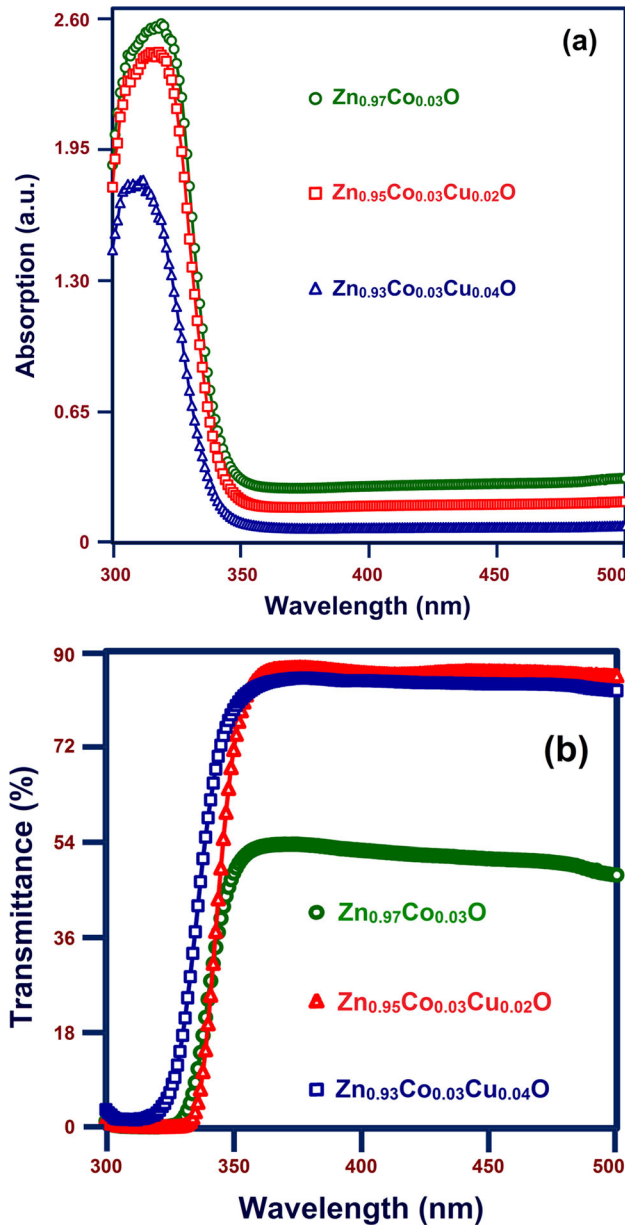
Fig. 7 UV–Visible **a** absorption spectra and **b** transmittance spectra of $Zn_{0.97-x}Co_{0.03}Cu_xO$ nanostructures with different Cu doping levels from 0 to 4% from 300 to 500 nm

transmittance is mostly due to the reflection of radiation. The highest transmittance ($\approx$ 88%) is achieved at Cu = 2%, and the further increase in Cu slightly decreases the transmittance. In addition to the change in transmittance, the absorption edge is shifted to higher wavelength side by Cu addition. The reduced transmittance at Cu—4% may be due to the existence of more lattice defects in Zn–O lattice [92].

3.5 Band gap estimation

Energy gap of the semiconducting materials is depending upon the different factors such as crystallite size, free charge carrier density and stress/strain [93]. The energy gap of the prepared samples was attained from $(\alpha h\nu)^2$ versus $h\nu$ plot by using the Tauc equation [94], $\alpha h\nu = A(h\nu - E_g)^{n/2}$, here, A is a constant, and E_g is the energy gap. Figure 8a presents the plot among $(\alpha h\nu)^2$ and $h\nu$ for the E_g assessment. It is analyzed by the extrapolation of the linear part of the $(\alpha h\nu)^2$ to the intersection with $h\nu$ portion as demonstrated in Fig. 8a. The plot among crystallite size and the energy gap for Cu = 0% to 4% is presented in Figs. 8b.

The resultant energy gap of Co-added ZnO ($Zn_{0.97}Co_{0.03}O$) is 3.63 eV which is greater than pure ZnO (3.37 eV). The noticed higher energy gap in the current investigation is owing to the size effect [95]. During the substitution of Cu = 2% into $Zn_{0.97-}Co_{0.03}O$ ($Zn_{0.95}Co_{0.03}Cu_{0.02}O$), the band gap is slightly increased to 3.66 eV, and here the change is very small. Usually, the energy gap of the material can be modified by the change in structure and the size of the material and the density of defects by impurity atoms [96]. The structural and the size variation in Zn–Co–O lattice by Cu = 2% addition as represented in Fig. 5 and 8b may cause the above slight elevation in E_g.

The further addition of Cu (Cu = 4%) moves the E_g to higher side. The detected blue shift of E_g throughout Cu levels between 0 and 4% is clarified by Burstein–Moss (BM) effect [97] as revealed in Fig. 8c. At higher Cu content, Fermi level shifts toward the conduction band by the induced free charge carrier as shown in Fig. 8c. By filling up the conduction energy level, charge transitions take place between the valence band and Fermi level in the conduction band as an alternative of valence and the bottom of the conduction bands. The above transitions shift the absorption edge toward the higher energy (blue shift) and elevate the energy gap [98] to higher value. The increase in energy gap by BM effect was described in the literature [99–101].

Generally, the size and energy gap are opposite to each other. At lower Cu level (Cu = 2%), the E_g is elevated to higher side, but the size is reduced to lower level which obeys the size effect [72]. This basic trend is deviated at higher Cu levels where the size and the E_g are increased to higher value side as
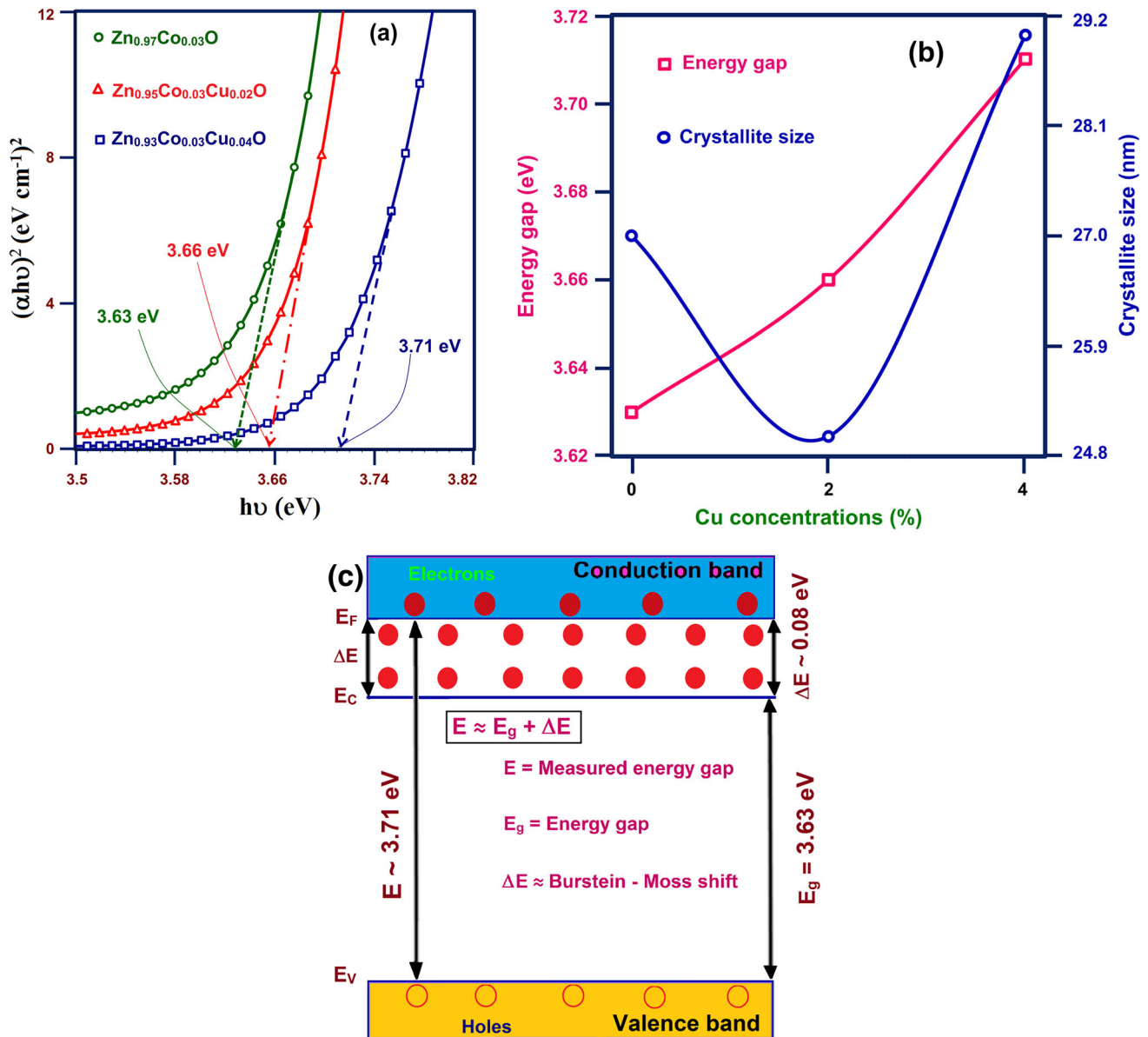
Fig. 8 a The $(\alpha h\upsilon)^2$ versus $h\upsilon$ curves for the energy gap calculation, **b** the variation of average crystallite size and energy gap of $Zn_{0.97-x}Co_{0.03}Cu_xO$ nanostructures with different Cu doping levels from 0 to 4%, **c** energy-level diagram to explain blue shift of energy by Burstein–Moss effect at $Zn_{0.93}Co_{0.03}Cu_{0.04}O$

illustrated in Fig. 8b. In view of the fact that the size of particles is higher than the excitonic Bohr radius, so the effect of size is negligible in the energy gap modification. The addition of higher Cu level induces the generation of different defect centers (Cu_{Zn}, Cu_i) by replacing either substitutional or interstitial Zn atoms in Zn-Co–O lattice which stimulate more structural deformations [102–104]. Therefore, it is suggested that the inclusion of Cu = 4% into Zn-Co–O modifies the structure and creates the more defects

[73] which is responsible for the elevation of both size and E_g.

3.6 FTIR analysis: Chemical bonding

The chemical bonding, the fundamental functional groups and the basic elements present in the materials are investigated by FTIR spectra. Figure 9 expresses the FTIR spectral analysis of $Zn_{0.97}Co_{0.03}O$, $Zn_{0.95}Co_{0.03}Cu_{0.02}O$ and $Zn_{0.93}Co_{0.03}Cu_{0.04}O$ nanostructures in the wave number range from 400 to
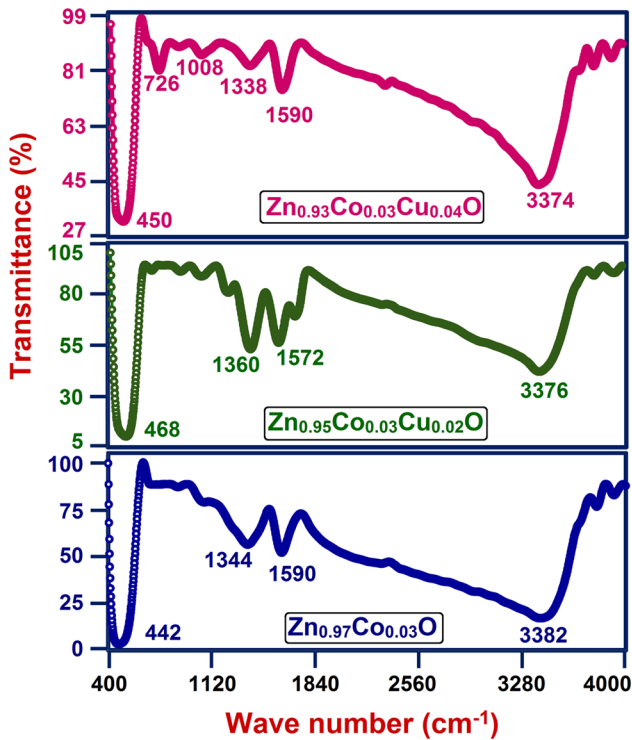
Fig. 9 FTIR spectra of $Zn_{0.97-x}Co_{0.03}Cu_xO$ nanostructures with different Cu doping levels from 0 to 4% from 400 to 4000 cm^{-1}

$4000 \ cm^{-1}$. The IR frequencies and their corresponding vibrational assignments of $Zn_{0.97-x}Co_{0.03-}Cu_xO$ ($0 \leq x \leq 0.04$) nanostructures at room temperature are presented in Table 5. The major and prominent signals detected between 3500 cm^{-1} and 3800 cm^{-1} may be payable to the stretching of polymeric hydroxyl groups (O–H) vibrations of H_2O in Cu/Co–Zn–O lattice [105, 106]. The missing band around 2400 cm^{-1} associated with the stretching mode of atmospheric CO_2 molecules in air confirms the absence of CO_2 in the material [107]. The IR bands about 1572–1590 cm^{-1} are accountable for O–H bending vibration [108].

The noticed moderate peaks around 1338–1360 cm^{-1} are due to the vibration of C = O

bonds [109]. The weak bands between 700 cm^{-1} and 1100 cm^{-1} represent the vibrations related to the stimulated defects and local bonds provoked by Cu in Zn–Co–O lattice [110–112] which are absent in $Zn_{0.97}Co_{0.03}O$. The bands below 700 cm^{-1} are generally originated from metal oxide (M–O) bonding. It is understand from the literature that the peaks about 600–650 cm^{-1} stand for tetrahedral co-ordinates and the peaks around 400–5000 cm^{-1} represent octahedral co-ordinates corresponding to the stretching vibration mode of Zn–O [113]. The noticed strong absorption peaks between 442 and 468 cm^{-1} in the current investigation confirm Zn–O stretching vibration with octahedral co-ordination. The modification in peak intensity and peak position around M–O bonding reflects the substitution of Co/Cu in ZnO, and this change is owing to the difference in bond lengths by Zn^{2+} ions restored by Co^{2+}/Cu^{2+} with dissimilar ionic radius [114].

3.7 Photoluminescence (PL) studies

The PL spectra of $Zn_{0.97}Co_{0.03}O$, $Zn_{0.95}Co_{0.03}Cu_{0.02}O$ and $Zn_{0.93}Co_{0.03}Cu_{0.04}O$ nanostructures between 350 and 600 nm at room temperature are as shown in Fig. 10a. Co-doped ZnO without Cu concentrations ($Zn_{0.97}Co_{0.03}O$) demonstrates four distinct PL emissions; the first emission around 390 nm ($E_g \sim 3.19$ eV) represents UV radiation, the second emission around 417 nm ($E_g \sim 2.98$ eV) stands for violet radiation, the third emission around 480 nm ($E_g \sim 2.59$ eV) corresponds to blue radiation, and the fourth emission around 525 nm ($E_g \sim 2.37$ eV) signifies the green radiation as pointed out in Fig. 10a.

The fundamental and the strong UV luminescence originated from the recombination of charges among the conduction band and valence band which is known as near-band edge (NBE) luminescence [115]. The visible near-violet emission at 2.98 eV (~ 417 nm) is due to the transition of electrons from

Table 5 IR peaks and their assignments of $Zn_{0.97-x}Co_{0.03}Cu_xO$ ($0 \leq x \leq 0.04$) nanostructures

| Assignments	Wave number (cm^{-1})		
	$Zn_{0.97}Co_{0.03}O$	$Zn_{0.95}Co_{0.03}Cu_{0.02}O$	$Zn_{0.93}Co_{0.03}Cu_{0.04}O$
O–H stretching vibration of H_2O	3382	3376	3374
H–O–H bending vibration	1590	1572	1590
Vibration of C = O bonds	1344	1360	1338
Micro-structural changes	–	1010	1008, 726
Stretching mode of Zn–O	442	468	450
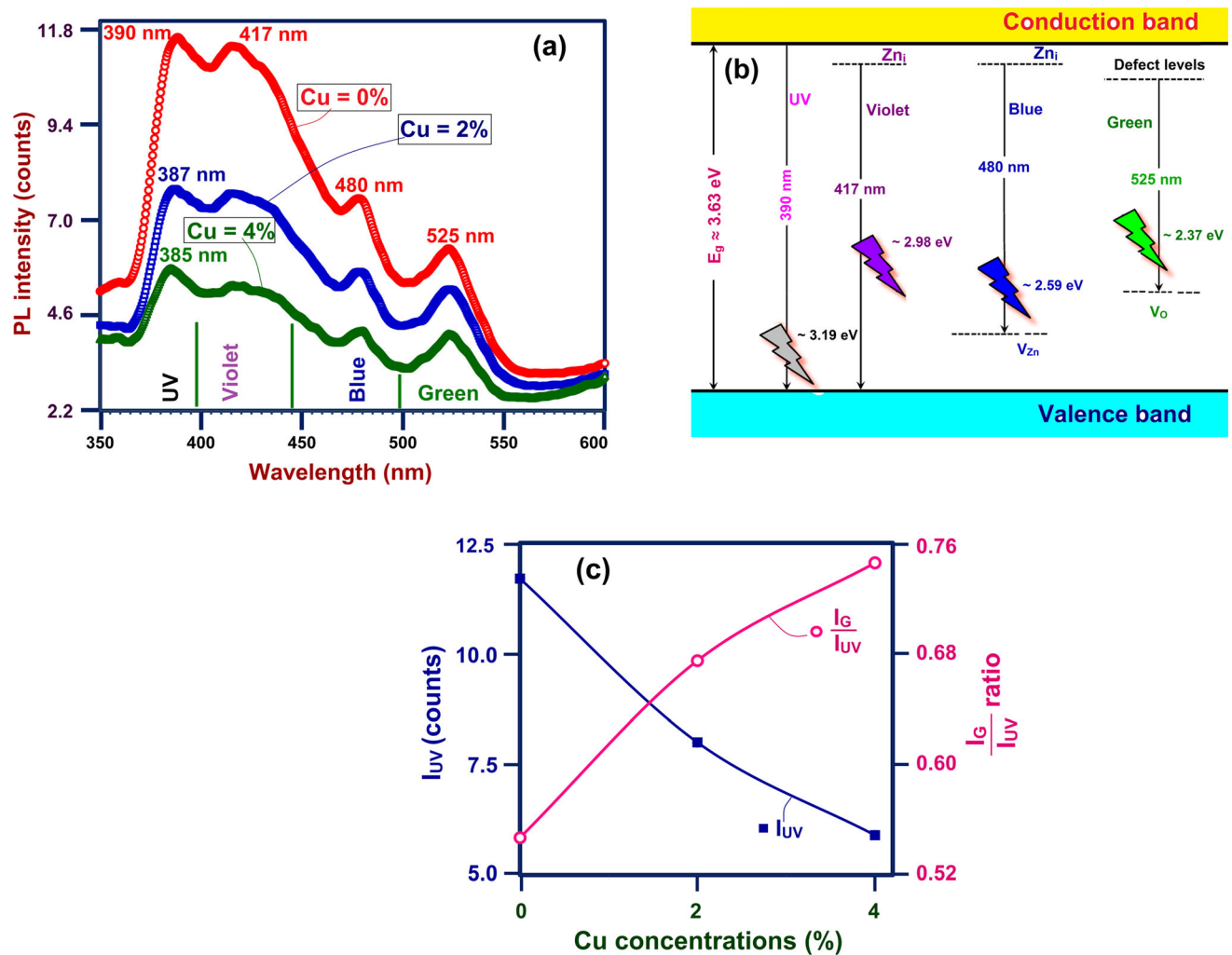
Fig. 10 a The room temperature PL spectra of $Zn_{0.97-x}Co_{0.03}Cu_xO$ nanostructures with different Cu doping levels from 0 to 4% as a function of wavelength between 350 and 600 nm, **b** the energy-level diagram to describe the UV, violet, blue and green light emissions in $Zn_{0.987}Co_{0.03}O$, **c** the variation of ultra-violet intensity and the intensity ratio between the green and ultra-violet emissions for different Cu levels from 0 to 4%

zinc interstitial (Zn_i) state to the top of the valence band (E_V). The visible blue emission found at 2.59 eV ($\sim$ 480 nm) is assigned to the charge transitions among zinc interstitial (Zn_i) near-conduction band and zinc vacancies (V_{Zn}) near-valence band [116]. The green emission at $\sim$ 2.37 eV ($\sim$ 525 nm) is due to the transition between shallowly trapped electron and a intensely trapped hole in singly/doubly ionized oxygen vacancies (V_O^+ / V_O^{++}) [117]. The similar green luminescence due to the transition of charges between the holes and V_O^+/V_O^{++} was reported by Vanheusden et al. [118] in ZnO phosphor. The typical energy-level diagram to explain the various luminescence like UV, violet, visible blue and

green radiation in $Zn_{0.97}Co_{0.03}O$ is presented in Fig. 10b.

When Cu is introduced into Zn–Co–O lattice, the intensity of both the UV and the visible near-violet emissions dropped to lower level with the increase in Cu concentrations. In addition to the intensity decline, the UV peaks are slightly shifted toward the lower wavelength side (blue shift) by Cu addition which is due to the alteration in electronic structure and also the energy gap of Cu-doped material [119]. The reported shrinkage in intensity is related to the size difference between the dopant and host elements which created the intrinsic defects in the basic lattice which are responsible for the improved visible luminescence [72].
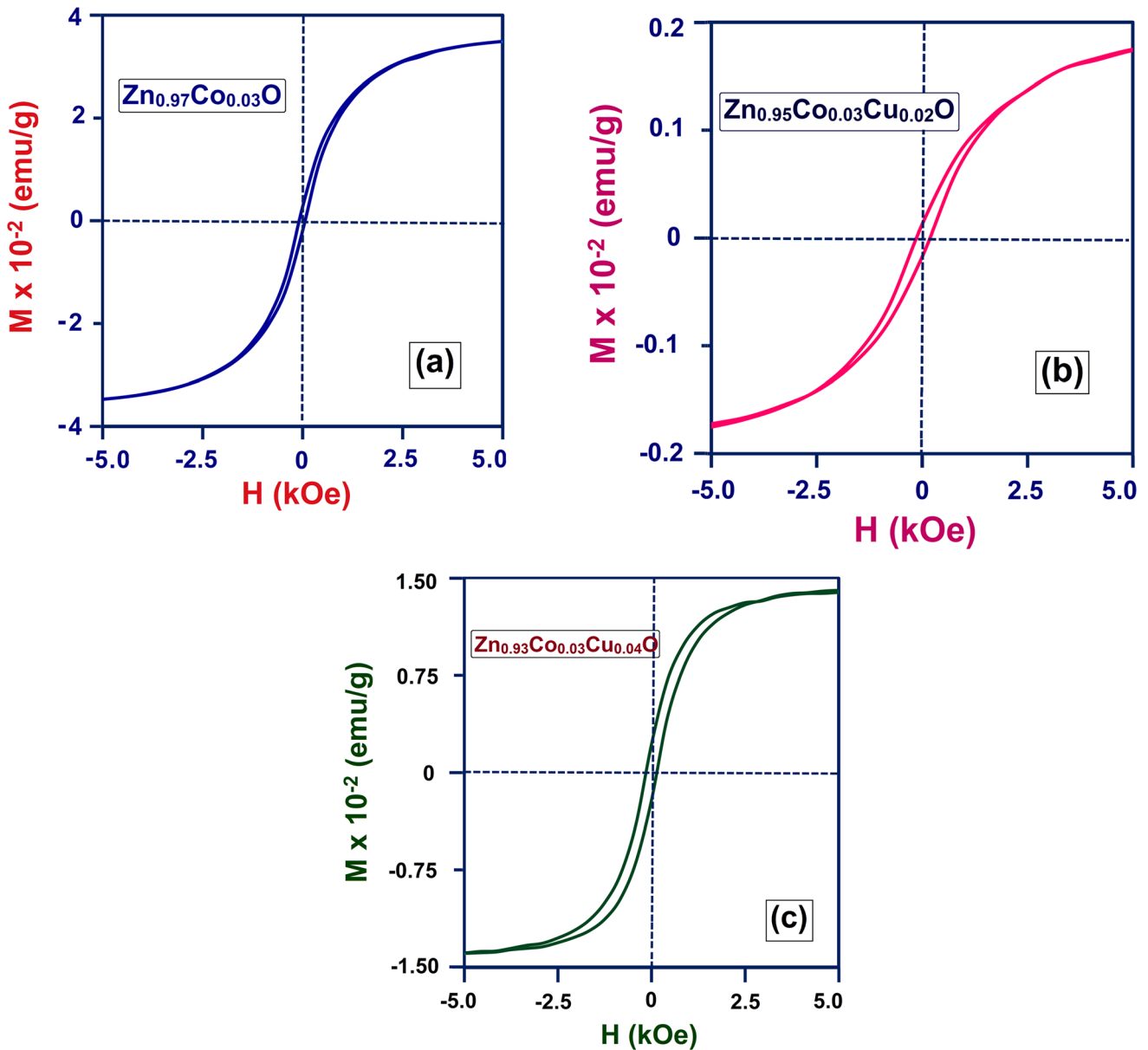
Fig. 11 Magnetization versus magnetic field (M–H) curves of **a** $Zn_{0.97}Co_{0.03}O$, **b** $Zn_{0.95}Co_{0.03}Cu_{0.02}O$ and **c** $Zn_{0.93}Co_{0.03}Cu_{0.04}O$ at room temperature

Figure 10 c represents the variation in UV emission intensity and the intensity ratio between green and UV light as a function of Cu concentrations from 0 to 4%. The UV emission intensity decreased continuously with Cu level, but the intensity ratio (I_G/I_{UV}) of green to UV peaks becomes greater during the increase in Cu levels from 0 to 4%. The effective increase in I_G/I_{UV} ratio with Cu addition as seen in Fig. 10c is owing to the generation of more defects such as oxygen vacancies and zinc vacancies [72, 120].

3.8 Magnetic properties

Figure 11a–c illustrates the alteration in magnetization for various Cu levels from 0 to 4% by varying the applied magnetic field (M–H) from − 5000 to + 5000 Oe at 300 K. Although the entire samples exhibit room temperature ferromagnetic (RTFM) behavior, the magnetization of Cu, Co dual-doped ZnO is less than Co-doped ZnO. Generally, the RTFM in the semiconducting material is achieved from the two different sources like the bound magnetic polarons
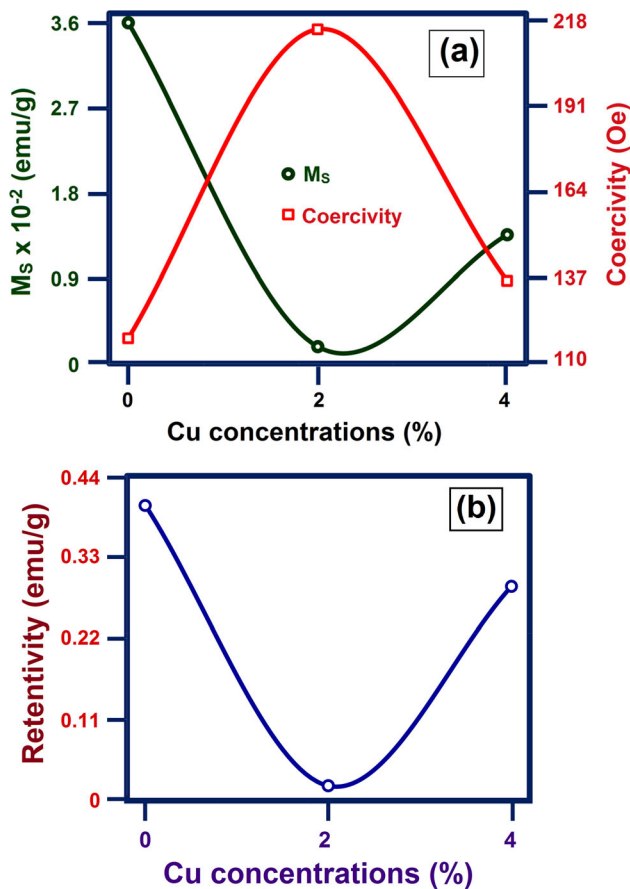
Fig. 12 a The variation in saturation magnetization (M_S) and coercivity and **b** the variation in retentivity for different Cu levels from 0 to 4% of $Zn_{0.97-x}Co_{0.03}Cu_xO$ nanostructures

(BMP) induced by point defects [121] and the exchange coupling between spin-polarized electrons and conductive electrons [122].

Khare et al. [123] investigated the magnetic properties of Co-doped ZnO and reported the effect of Zn interstitials in the origin of RTFM. They discussed that the noticed magnetization in Co-added ZnO is improved by the Zn interstitials in the Zn–O lattice by annealing, but not depending on carrier concentrations. But, Ahmed et al. stated that the RTFM in TM-doped ZnO is not only by the magnetic moment of the TM ions but also by existing free electrons [124]. The substitution of Cu (Cu = 2%) into $Zn_{0.97}Co_{0.03}O$ nanostructures moderately suppresses the magnetization. The elevated anti-ferromagnetic (AFM) coupling among neighboring Cu–Cu ions decreased the FM at Cu = 2% [125]. Moreover, the size reduction in the material (nanonature) and the slowing inter-particle exchange are also responsible for the present decrease in magnetization [126].

Figure 12a shows the modification along the saturation magnetization (M_S) and the coercivity for different Cu doping level from 0 to 4%. Figure 12b illustrates the retentivity for different Cu doping level from 0 to 4%. The decreasing M_S and retentivity at Cu = 2% are displayed in Fig. 12. During increase in Cu level from 2 to 4%, the magnetization and retentivity are slightly increased which may be due to the existence of more number of oxygen vacancies (V_o). The PL studies from Fig. 10 confirmed the presence of much oxygen-related defects at Cu = 4% which initiate defect-associated hybridization and stimulate a long-range ferromagnetic ordering [127, 128] and hence retentivity increased, but coercivity get declined. At higher Cu concentrations, the local density of states (DOS) is improved by increasing local holes at anion sites at the Fermi level which enhanced the exchange interaction [40]. This is also one more reasons to enhance the M_S at Cu = 4%. The diminishing coercivity and a small-level improvement in retentivity at Cu = 4% as noted from Fig. 12 are owing to the high density defects particularly oxygen-related defects. Moreover, the absence of secondary/impurity phases of Co/Cu in Zn–Co–Cu–O lattice detected from XRD analysis confirmed that the existing FM order in Co/Cu-doped ZnO is simply by the intrinsic nature.

4 Conclusions

Following are the conclusions drawn from the present investigation:

- Co-doped ZnO and Co and Cu dual-doped ZnO nanostructures were synthesized using the co-precipitation technique.
- The structural analysis showed that no modification in the structure of hexagonal ZnO and the also the nonexistence of secondary/impurity phases were observed by Co/Cu doping into ZnO.
- The reduction of crystallite size ($\approx$ 25 nm) at Cu = 2% is due to the suppression of growth rate and the dissimilarities between Co^{2+}/Cu^{2+} and Zn^{2+} ions, and the enhanced crystallite size ($\approx$ 29 nm) at Cu = 4% is responsible for the more defect sites associated with interstitials and vacancies of Co^{2+} and Cu^{2+} in Zn–O lattice.

- The persistent c/a ratio ($\sim$ 1.602) signified the absence of structural modification by Co/Cu substitution for Zn.
- The changes in optical absorption, transmittance and energy gap of ZnO by Co/Cu doping were discussed by consideration of dopants and the stimulated defect states.
- The lower crystallite size ($\sim$ 25 nm) and the higher optical transmittance characteristic of $Zn_{0.95}Co_{0.03}Cu_{0.02}O$ nanostructure are useful for the production of efficient industrial transparent electrodes.
- The constant broadening of energy gap with Cu doping is explained using Burstein–Moss (BM) band filling effect with the help of energy-level diagram.
- The existence of Zn–O and Zn–Co/Cu–O bonding was verified by Fourier transform infrared analysis.
- The elevated intensity ratio between green and ultra-violet photoluminescence (I_G/I_{UV}) at higher Cu concentrations revealed the occurrence of higher number of defects, particularly oxygen-related defect states, in (Zn, Co, Cu)O lattice.
- Tuning of crystallite size, energy gap and photo-luminescence characteristics of $Zn_{0.97}Co_{0.03}O$ nanostructures by Cu doping is helpful for the opto-electronic device applications.
- The observed RTFM in Co, Cu-doped ZnO nanostructures was discussed based on the oxygen vacancy-mediated bound magnetic polarons (BMP) and the exchange coupling among the free electrons and local spin-polarized electrons.

References

1. S. Zinatloo-Ajabshir, M. Baladi, M. Salavati-Niasari, Ultrason. Sonochem. **72**, 105420 (2021)
2. M. Mousavi-Kamazani, S. Zinatloo-Ajabshir, M. Ghodrati, J. Mater. Sci.: Mater. Electron. **31**, 17332–17338 (2020)
3. S. Zinatloo-Ajabshir, N. Ghasemian, M. Mousavi-Kamazani, M. Salavati-Niasari, Ultrason. Sonochem. **71**, 105376 (2021)
4. S. Zinatloo-Ajabshir, M.S. Morassaei, O. Amiri, M. Salavati-Niasari, Ceram. Int. **46**, 6095–6107 (2020)
5. S. AliHeidari-Asil, S. Zinatloo-Ajabshir, O. Amiri, M. Salavati-Niasari, Int. J. Hydrog. Energy **45**, 22761–22774 (2020)
6. S. Zinatloo-Ajabshir, M. Mousavi-Kamazani, Ceram. Int. **46**, 26548–26556 (2020)
7. S.N. Bai, T.Y. Tseng, J. Appl. Phys. **74**, 695–703 (1993)
8. M. Aslam, V.A. Chaudhary, I.S. Mulla, S.R. Sainkar, A.B. Mandale, A.A. Belhekar, K. Vijayamohanan, Sens. Actuators A Phys. **75**, 162–167 (1999)
9. O. Kluth, B. Rech, L. Houben, S. Wieder, G. Schope, C. Beneking, H. Wagner, A. Loffl, H.W. Schock, Thin Solid Films **351**, 247–253 (1999)
10. N.K. Zayer, R. Greef, K. Roger, A.J.C. Grellier, C.N. Pannell, Thin Solid Film **352**, 179–184 (1999)
11. S.J. Pearton, C.R. Abernathy, D.P. Norton, A.F. Hebard, Y.D. Park, L.A. Boatner, J.D. Budai, Mater. Sci. Eng. R **40**, 137–168 (2003)
12. F. Pan, C. Song, X.J. Liu, Y.C. Yang, F. Zeng, Mater. Sci. Eng. R **62**, 1–35 (2008)
13. D. Mocatta, G. Cohen, J. Schattner, O. Millo, E. Rabani, E. Rabani, U. Banin, Science **332**, 77–81 (2011)
14. R. Beaulac, L. Schneider, P.I. Archer, G. Bacher, D.R. Gamelin, Science **325**, 973–976 (2009)
15. J.M.D. Coey, M. Venkatesan, C.B. Fitzgerald, Nat. Mater. **4**, 173–179 (2005)
16. T. Dietl, H. Ohno, F. Matsukura, J. Cibert, D. Ferrand, Science **287**, 1019–1022 (2000)
17. S.A. Wolf, D.D. Awschalom, R.A. Buhrman, J.M. Daughton, S. von Molnár, M.L. Roukes, A.Y. Chtchelkanova, D.M. Treger, Science **294**, 1488–1495 (2001)
18. W. Chen, Y.H. Lu, M. Wang, L. Kroner, H.J. Fecht, J. Phys. Chem. C **113**, 1320–1324 (2009)
19. P.Y. Wang, Q.H. Gao, J.Q. Xu, Fine Chem. **24**, 436–440 (2007)
20. K. Sato, H. Katayama-Yoshida, Jpn. J. Appl. Phys. **39**, L555–L558 (2000)
21. K. Sato, H. Katayama-Yoshida, J. Appl. Phys. **40**, L334–L336 (2001)
22. J.J. Ding, H.X. Chen, X.G. Zhao, S.Y. Ma, J. Phys. Chem. Solids **71**, 346–350 (2010)
23. Z.Q. Ma, W.G. Zhao, Y. Wang, Thin Solid Films **515**, 8611–8614 (2007)
24. Z. Zhang, J.B. Yi, J. Ding, L.M. Wong, H.L. Seng, S.J. Wang, J.G. Tao, G.P. Li, G.Z. Xing, T.C. Sum, C.H.A. Huan, T. Wu, J. Phys. Chem. C **112**, 9579–9585 (2008)
25. J. Zhong, S. Muthukumar, Y. Chen, Y. Lu, Appl. Phys. Lett. **83**, 3401–3403 (2003)
26. T. Yamada, A. Miyake, S. Kishimoto, H. Makino, N. Yamamoto, T. Yamamoto, Surf. Coat. Technol. **202**, 973–976 (2007)
27. Y.M. Tao, S.Y. Ma, H.X. Chen, J.X. Meng, L.L. Hou, Y.F. Jia, X.R. Shang, Vacuum **85**, 744–748 (2011)
28. Z.B. Bahsi, A. Yavu Ozral, Opt. Mater. **29**, 672–678 (2007)

29. M. Arshad, A. Azam, A.S. Ahmed, S. Mollah, A.H. Naqvi, J. Alloys Compd. **509**, 8378–8381 (2011)

30. T. Wang, Y. Liu, Q. Fang, Y. Xu, G. Li, Z. Sun, M. Wu, J. Li, H. He, J. Alloys Compd. **509**, 9116–9122 (2011)

31. M. Nirmala, A. Anukaliani, Phys. B **406**, 911–915 (2011)

32. H.-J. Lee, G.H. Ryu, S.K. Kim, S.A. Kim, C.H. Lee, S.-Y. Jeong, C.R. Cho, Phys. Status Solidi **241**, 2858–2861 (2004)

33. D. Anbuselvan, S. Muthukumaran, M. Ashokkumar, J. Mater. Sci.: Mater. Electron. **25**, 2004–2015 (2014)

34. D. Chakraborti, S. Ramachandran, G. Trichy, J. Narayan, J. Appl. Phys. **101**, 053918 (2007)

35. D.L. Hou, X.J. Ye, H.J. Meng, H.J. Zhou, X.L. Li, Appl. Phys. Lett. **90**, 142502 (2007)

36. H. Xu, Q. Zhao, H. Yang, Y. Chen, J. Nanopart. Res. **11**, 615–621 (2009)

37. O.D. Jayakumar, I.K. Gopalakrishnan, S.K. Kulshreshtha, J. Mater. Chem. **15**, 3514–3518 (2005)

38. S. Zhang, F. Hu, J. He, W. Cheng, Q. Liu, Y. Jiang, Z. Pan, W. Yan, Z. Sun, S. Wei, J. Phys. Chem. C **117**, 24913–24919 (2013)

39. S. Vignesh, S. Suganthi, J.K. Sundar, V. Raj, P.R. Indra Devi, Appl. Surf. Sci. **479**, 914–929 (2019)

40. V. Shanmugam, K.S. Jeyaperumal, Appl. Surf. Sci. **449**, 617–630 (2018)

41. V. Shanmugam, K.S. Jeyaperumal, P. Mariappan, A.L. Muppudathi, New J. Chem. **44**, 13182–13194 (2020)

42. S. Vignesh, A.L. Muppudathi, J.K. Sundar, J. Mater. Sci.: Mater. Electron. **29**, 10784–10801 (2018)

43. V. Shanmugam, S. Sanjeevamuthu, J.K. Sundar, V. Raj, J. Ind. Eng. Chem. **76**, 318–332 (2019)

44. A. Baig, V. Rathinam, J. Palaninathan, J.Iran. Chem. Soc. (2020). https://doi.org/10.1007/s13738-020-02000-2

45. B.A. Baig, V. Rathinam, J. Palaninathan, Appl. Water Sci. **10**, 54 (2020). https://doi.org/10.1007/s13201-019-1119-1

46. H.T. Lin, T.S. Chin, J.C. Shih, S.H. Lin, T.M. Hong, R.T. Huang, F.R. Chen, J.J. Kai, Appl. Phys. Lett. **85**, 621–623 (2004)

47. Y. Wei, D. Hou, S. Qiao, C. Zhen, G. Tang, Phys. B **404**, 2486–2488 (2009)

48. S. Zinatloo-Ajabshir, Z. Salehi, O. Amiri, M. Salavati-Niasari, J. Alloys Compd. **791**, 792–799 (2019)

49. S. Zinatloo-Ajabshir, Z. Salehi, M. Salavati-Niasari, J. Clean. Prod. **215**, 480–487 (2019)

50. S. Zinatloo-Ajabshir, Z. Salehi, M. Salavati-Niasari, Ceram. Int. **44**, 3873–3883 (2018)

51. M. Sadatorassaei, S. Zinatloo-Ajabshir, M. Salavati-Niasari, J. Mater. Sci.: Mater. Electron **27**, 11698–11706 (2016)

52. S. Zinatloo-Ajabshir, Z. Salehi, M. Salavati-Niasari, Clean. Prod. **192**, 678–687 (2018)

53. L.-H. Ye, A.J. Freeman, B. Delley, Phys. Rev. B **73**, 033203 (2006)

54. S. Muthukumaran, R. Gopalakrishnan, Opt. Mater. **34**, 1946–1953 (2012)

55. M. Ferhat, A. Zaoui, R. Ahuja, Appl. Phys. Lett. **94**, 142502 (2009)

56. H. Liu, J. Yang, Z. Hua, Y. Zhang, L. Yang, L. Xiao, Z. Xie, Appl. Surf. Sci. **256**, 4162–4165 (2010)

57. B.D. Cullity, *Elements of X-Ray Diffraction*, 2nd edn. (Addison Wesley, Boston, 1978).

58. F.C. Hu, Z.Y. Pan, T. Yao, H. Oyanagi, Y. Jiang, W.S. Yan, B. He, J. Ye, S.Q. Wei, J. Phys. D Appl. Phys. **42**, 125408 (2009)

59. M. Mukhtar, L. Munisa, R. Saleh, Mater. Sci. Appl. **3**, 543–551 (2012)

60. X. Peng, J. Xu, H. Zang, B. Wang, Z. Wang, J. Lumin. **128**, 297–300 (2008)

61. A. Sreedhar, J.H. Kwon, J. Yi, J.S. Kim, J.S. Gwag, Mater. Sci. Semicond. Process. **49**, 8–14 (2016)

62. A.N. Kadam, T.G. Kim, D.S. Shin, K.M. Garadkar, J. Park, J. Alloys Compd. **710**, 102–113 (2017)

63. S.P. Meshram, P.V. Adhyapakn, D.P. Amalnerkar, I.S. Mulla, Ceram. Int. **42**, 7482–7489 (2016)

64. B. Babu, T. Aswani, G.T. Rao, R.J. Stella, B. Jayaraja, R.V.S.S.N. Ravikumar, J. Magn. Magn. Mater. **355**, 76–80 (2014)

65. V. Vaiano, G. Iervolino, L. Rizzo, Appl. Catal. B: Environ. **238**, 471–479 (2018)

66. D. Anbuselvan, S. Muthukumaran, Opt. Mater. **42**, 124–131 (2015)

67. Y. Liu, H. Liang, L.X. Jianze Zha, J. Bian, Y. Luo, Y. Liu, W. Li, G. Wu, G. Du, J. Appl. Phys. **108**, 113507 (2010)

68. S. Singhal, J. Kaur, T. Namgyal, R. Sharma, Phys. B Condens. Matter **407**, 1223–1226 (2012)

69. M. Öztas, M. Bedir, Thin Solid Films **516**, 1703–1709 (2008)

70. M. Ashokkumar, S. Muthukumaran, Powder Technol. **258**, 157–164 (2014)

71. S.A. Ahmed, Results Phys. **7**, 604–610 (2017)

72. M. Sajjad, I. Ullaha, M.I. Khanb, J. Khanc, M. Yaqoob Khana, M.T. Qureshi, Results Phys. **9**, 1301–1309 (2018)

73. P.K. Sharma, M. Kumar, A.C. Pandey, J. Nanopart. Res. **13**, 1629–1637 (2011)

74. G. Vijayaprasath, R. Murugan, S. Asaithambi, G. Anandha Babu, P. Sakthivel, T. Mahalingam, Y. Hayakawa, G. Ravi, Appl. Phys. A **122**, 122 (2016)

75. M.J. Chithra, K. Pushpanathan, Modern Phys. Lett. B **30**, 1650406 (2016)

76. J. Pelleg, E. Elish, J. Vac. Sci. Technol. A **20**, 754–761 (2002)

77. M. Sarfrazi, N. Ahmed, K. Ul-Haq, S. Shahida, M.A. Khan, Mater. Sci. Poland **37**, 280–288 (2019)

78. D. Theyvaraju, S. Muthukumaran, Phys. E **74**, 93–100 (2015)

79. M. Ashokkumar, S. Muthukumaran, Superlattices Microstruct. **69**, 53–64 (2014)

80. U. Ozgur, Y. Alivov, C. Liu, A. Teke, M.A. Reshchikov, S. Dogan, V.A. Cho, H. Morkoc, J. Appl. Phys. **98**, 041301–041402 (2005)

81. Y. Liu, J. Yang, Q. Guan, L. Yang, Y. Zhang, Y. Wang, B. Feng, J. Cao, X. Liu, Y. Yang, M. Wei, J. Alloys Compd. **486**, 835–838 (2009)

82. H. Liu, J. Yang, Z. Hua, Y. Liu, L. Yang, Y. Zhang, J. Cao, Mater. Chem. Phys. **125**, 656–659 (2011)

83. L. Chow, O. Lupan, G. Chai, H. Khallaf, L. K. Ono, B. Roldan Cuenya, I. M. Tiginyanu, V. V. Ursaki, V. Sontea, A. Schulte, Sens. Actuators B **189**:399–409 (2013)

84. R. Sangeetha, S. Muthukumaran, M. Ashokkumar, Spectrochim. Acta A: Mol. Biomol Spectrosc. **144**, 1–7 (2015)

85. J.A. Mary, J.J. Vijaya, M. Bououdina, L. Kennedy, J.H. Dai, Y. Song, Phys. E **66**, 209–220 (2015)

86. J.H. Lang, X. Lia, J.H. Yang, L.L. Yang, Y.J. Zhang, Y.S. Yan, Q. Han, M.B. Wei, M. Gao, X.Y. Liu, R. Wang, Appl. Surf. Sci. **257**, 9574–9577 (2011)

87. L.F. Koao, F.B. Dejene, H.C. Swart, J.R. Botha, J. Lumin. **143**, 12–17 (2013)

88. L. Zhang, Y. Yang, R. Fan, J. Yu, L. Li, J. Mater. Chem. A **1**, 12066–12073 (2013)

89. A. Azam, A.S. Ahmed, M.S. Ansari, M. Shafeeq, A.H. Naqvi, J. Alloys Compd. **506**, 237–242 (2010)

90. M.L. Singla, M.M. Shafeeq, M. Kumar, J. Lumin. **129**, 434–438 (2009)

91. A.J. Reddy, M.K. Kokila, H. Nagabhushana, R.P.S. Chakradhar, C. Shivakumar, J.L. Rao, B.M. Nagabhushana, J. Alloys. Compd. **509**, 5349–5355 (2011)

92. Y.H. Hu, Y.C. Chen, H.J. Xu, H. Gao, W.H. Jiang, F. Hu, Y.X. Wang, Engineering **2**, 973–978 (2010)

93. T.M. Hammad, J.K. Salem, R.G. Harrison, R. Hempelmann, N.K. Hejazy, J. Mater. Sci. Mater. Electron. **24**, 2846–2852 (2013)

94. M. Masjedi-Arani, M. Salavati-Niasari, J. Mol. Liq. **248**, 197–204 (2017)

95. A.P. Palomino, O.P. Perez, R. Singhal, M. Tomar, J. Wang, P.M. Voyles, J. Appl. Phys. **103**, 07121 (2008)

96. S. Suwanboon, P. Amornpitoksuk, P. Bangrak, A. Sukolrat, N. Muensit, J. Ceram. Process Res. **11**, 547–551 (2010)

97. E. Burstein, Phys. Rev. **93**, 632–633 (1954)

98. S. Kumar, S. Chatterjee, K.K. Chattopadhyay, A.K. Ghosh, J. Phys. Chem. C **116**, 16700–16708 (2012)

99. K. Sakai, T. Kakeno, T. Ikari, S. Shirakata, T. Sakemi, K. Awai, T. Yamamoto, J. Appl. Phys. **99**, 043508–043514 (2006)

100. K. Rekha, M. Nirmala, M. Nair, A. Anukaliani, Phys. B **405**, 3180–3185 (2010)

101. K. Joshi, M. Rawat, S.K. Gautam, R.G. Singh, R.C. Ramola, F. Singh, J. Alloys Compd. **680**, 252–258 (2016)

102. N.Y. Garces, L. Wang, L. Bai, N.C. Giles, L.E. Halliburton, G. Cantwell, Appl. Phys. Lett. **81**, 622–624 (2002)

103. S.Y. Li, P. Lin, C.Y. Lee, T.Y. Tseng, J. Appl. Phys. **95**, 3711–3716 (2004)

104. K. Yamamoto, K. Nagasawa, T. Ohmori, Phys. E Low. Dimens. Syst. Nanostruct. **24**, 129–132 (2004)

105. C. Malarkodi, S. Rajeshkumar, K. Paulkumar, M. Vanaja, G. Gnanajobitha, G. Annadurai, Bioinorg. Chem. Appl. **2014**, 347167 (2014)

106. S. Pulipati, S.H. Parveen, R.K. Babu, J. Pharmacogn. Phytochem. **2**, 189–192 (2013)

107. Z.A. Fattah, Int. J. Eng. Sci. Res. Technol. **5**(7), 418–429 (2016)

108. K. Nakamoto, *Infrared and Raman Spectra of Inorganic and Coordination Compounds, Parts-A and B* (Wiley, New York, 1997).

109. S. Senthilkumar, K. Rajendran, S. Banerjee, T.K. Chini, V. Sengodan, Mater. Sci. Semicond. Process **11**, 6–12 (2008)

110. R. Elilarassi, G. Chandrasekaran, Mater. Chem. Phys. **123**(2–3), 450–455 (2010)

111. R.N. Aljawfi, S. Mollah, J. Magn. Magn. Mater. **323**, 3126–3132 (2011)

112. N. Goswami, A. Sahai, Mater. Res. Bull. **48**, 346–351 (2013)

113. R.D. Waldron, Phys. Rev. **99**, 1727 (1955)

114. K.P. Shinde, R.C. Pawar, B.B. Sinha, H.S. Kim, S.S. Oh, K.C. Chung, Ceram. Int. **40**, 16799–16804 (2014)

115. A.S. Kumar, N.M. Huang, H.S. Nagaraja, Electron. Mater. Lett. **10**, 753–758 (2014)

116. D. Raoufi, J. Lumin. **134**, 213–219 (2013)

117. S. Monticone, R. Tufeu, A.V. Kanaev, J. Phys. Chem. B **102**, 2854–2862 (1998)

118. K. Vanheusden, W.L. Warren, C.H. Seager, D.R. Tallant, J.A. Voigt, B.E. Gnade, J. Appl. Phys. **79**, 7983 (1996)

119. J.H. He, C.S. Lao, L.J. Chen, D. Davidovic, Z.L. Wang, J. Am. Chem. Soc. **127**, 16376 (2005)

120. B. Lin, Z. Fu, Y. Jia, Appl. Phys. Lett. **79**, 943 (2001)

121. T.S. Herng, S.P. Lau, S.F. Yu, J.S. Chen, K.S. Teng, J. Magn. Magn. Mater. **315**, 107–110 (2007)

122. C.H. Xia, C.G. Hu, C.H. Hu, Z. Ping, F. Wang, Bull. Mater. Sci. **34**, 1083–1087 (2011)

123. N. Khare, M.J. Kappers, M. Wei, M.G. Blamire, J.L. MacManus-Driscoll, Adv. Mater. **18**, 1449–1452 (2006)

124. F. Ahmed, S. Kumar, N. Arshi, M.S. Anwar, S.N. Heo, B.H. Koo, Acta Mater. **60**, 5190–5196 (2012)

125. P.K. Sharma, R.K. Dutta, A.C. Pandey, J. Magn. Magn. Mater. **321**, 4001–4005 (2009)

126. D. Karmakar, S.K. Mandal, R.M. Kadam, P.L. Paulose, A.K. Rajarajan, T.K. Nath, A.K. Das, I. Dasgupta, G.P. Das, Phys. Rev. B **75**, 144404 (2007)

127. G.Z. Xing, D.D. Wang, J.B. Yi, L.L. Yang, M. Gao, M. He, J.Y. Yang, J. Ding, T.C. Sum, T. Wu, Appl. Phys. Lett. **96**, 112511 (2010)

128. Y.F. Li, R. Deng, B. Yao, G.Z. Xing, D.D. Wang, T. Wu, Appl. Phys. Lett. **97**, 102506 (2010)